International Journal of Heat and Mass Transfer 139 (2019) 588–599

Contents lists available at ScienceDirect

International Journal of Heat and Mass Transfer

journal homepage: www.elsevier.com/locate/ijhmt

Lattice Boltzmann study of pool boiling heat transfer enhancement on structured surfaces

Xiangting Chang [a], Haibo Huang [a,*], Yong-Pan Cheng [b], Xi-Yun Lu [a]

[a] Department of Modern Mechanics, University of Science and Technology of China, Hefei 230026, China
[b] School of Energy, Power and Mechanical Engineering, North China Electric Power University, Beijing 102206, China

ARTICLE INFO

Article history:
Received 14 February 2019
Received in revised form 13 May 2019
Accepted 15 May 2019

Keywords:
Boiling
Heat transfer enhancement
Structured surfaces
Lattice Boltzmann method

ABSTRACT

Pool boiling heat transfer enhancement on structured surfaces with columns is investigated by a thermal two-phase lattice Boltzmann model. The effects of geometrical parameters, including column height (H), width (W) and gap spacing (D), are discussed in detail. The size of columns is comparable to the diameter of a typical detached bubble (d_b). It is found that the heat transfer performance mainly depends on two factors: the heated surface area A and local convective flow field. When W and D are properly chosen as about $W = D \approx 4d_b$, increasing H enhances the heat transfer solely due to the increase of the surface area. When W and D are small, it is observed that the top of the columns and the channels are mostly covered by a layer of vapor, respectively, which weaken the convection. Under the circumstances, although surface area A increases, heat transfer enhancement is not so significant. For the surface tension effect, the enhancement of the structured surface decreases with the increase of capillary number compared to that of the plain surface. The mechanism is that at larger capillary number, the convection close to the channel may be partially blocked, which hinders the heat transfer. An optimal enhancement could be achieved when A is as large as possible and meanwhile the convection is not hindered by the bubbles behaviors. The finding here may shed some light on mechanism of heat transfer enhancement on structured surfaces with columns.
© 2019 Elsevier Ltd. All rights reserved.

1. Introduction

Pool boiling heat transfer is an efficient heat transfer mode during the phase change from liquid to vapor. It has been widely used in industrial production and daily life. In order to further improve the heat transfer performance, numerous enhanced surfaces have been designed and adopted, such as biphilic surfaces, biconductive surfaces, and structured surfaces [1]. Among them, the structured surface is easy to process and it is an effective way to enhance heat transfer. During the past few years, a lot of experimental works have been carried out to study pool boiling heat transfer enhancement on structured surfaces [2–6]. For example, Cooke et al. [2] evaluated the heat transfer capabilities of different surface geometries on a silicon chip. They found that surfaces with microchannels are efficient for boiling heat transfer because the surfaces allow liquid to flow through the open channels and wet the heat transfer surface. Chu et al. [5] studied effect of surface roughness-augmented wettability on critical heat flux (CHF) during pool boiling. An analytical force-balance model was extended to explain the CHF enhancement. However, in these experimental studies, most of them first measured the boiling curves, and then conjectured or proposed a reasonable mechanism for the change in heat transfer performance. In some literatures [2–4], researchers attempted to capture bubble dynamics using the high-speed cameras to further understand the mechanism, but most of results are not so satisfactory due to the limitations of experimental observation techniques. Meanwhile, flow field visualization is also difficult. So the mechanism and heat transfer characteristics for pool boiling on structured surfaces are not well understood. On the other hand, computational fluid dynamics (CFD) is able to provide more details, and it is a powerful tool to promote the understanding of the inherent mechanism of the boiling heat transfer enhancement on structured surfaces.

Many numerical simulations have been carried out to study pool boiling [7,8], while numerical investigations of heat transfer enhancement due to structured surfaces have rarely been reported. For example, Zhou et al. [9] studied the performance of a micro-pillar structure combined with an engineered wettability pattern. In the study, the heterogeneous boiling and heat transfer enhancement were investigated using a volume of fluid (VOF) method. The effects of the wettability texture on two-phase flow dynamics and heat transfer characteristics were revealed. Zhao et al. [10] used a two-dimensional VOF method to analyze the pool boiling heat transfer on the heated surfaces with different

* Corresponding author.
E-mail address: huanghb@ustc.edu.cn (H. Huang).

https://doi.org/10.1016/j.ijheatmasstransfer.2019.05.041
0017-9310/© 2019 Elsevier Ltd. All rights reserved.

microstructures size and mixed hydrophilic and hydrophobic areas. However, the VOF method has to track or reconstruct the vapor-liquid interface and is not able to describe the entire ebullition of the bubble cycles [11].

In recent years, the lattice Boltzmann method (LBM) has received extensive attention and been widely used to simulate complex multiphase systems [12,13]. It is a mesoscopic method based on the discrete Boltzmann equation. Comparing with conventional methods for multiphase flows, the LBM does not track interfaces explicitly while sharp interfaces can be maintained. In particular, The Shan-Chen pseudo-potential lattice Boltzmann (LB) model [14] is able to simulate thermal two-phase flows [15–21] and has become the most popular multiphase LB model. Using the model, quantitative analyses for the bubble departure from a horizontal plate in heterogeneous boiling were carried out by Házi et al. [16] The model was also applied to study bubble behaviors in presence of a heated wall by Cheng et al. [18,22,23] Quantitative validation of the pseudo-potential phase change model in boiling simulation is provided [22] and the LBM simulation results of both film boiling heat transfer rate and CHF were consistent with those obtained from classical theoretical models [23]. The three dimensional (3D) thermal pseudo-potential model was applied to simulate the turbulent convection in multiphase flows [17].

For boiling on structured surfaces, Márkus et al. [24] studied the effects of various factors including heat flux, wettability, and cavity size on bubble growth and departure. Gong et al. [25] studied bubble nucleation, growth, departure from multi-cavities and interactions of the bubbles. In the above studies, heat transfer enhancement has never been discussed in detail. Li et al. [26] investigated the boiling heat transfer enhancement on hydrophilic-hydrophobic mixed surfaces. However, they mainly evaluated the influence of mixed wettability rather than the structure itself. Furthermore, in most of the LBM studies of boiling on structured surfaces, the conjugate fluid-solid heat transfer condition is ignored. Actually, the conjugate heat transfer condition is important for the heated solid wall [27]. Wall temperature oscillation due to spatial and temporal variation in heat transfer on the fluid side may affect bubble generation [27]. Meanwhile, the conjugate heat transfer condition is able to determine the thermal response of the solid.

Recently, Mu et al. [11] discussed the effect of cavity shapes on boiling heat transfer and they applied the conjugate heat transfer condition in their simulations. However, in their study, only bubble behaviors and heat transfer characteristics were concerned without paying attention to the mechanism of heat transfer enhancement. In the above studies, the performance of structured surfaces is seldom compared to that of the plain surface [24,28,25,26,11]. Besides, the effect of surface tension has never been studied.

In this paper, boiling heat transfer performance on structured surfaces with columns are investigated. A fluid-solid conjugate heat transfer interface condition for generalized interfaces is imposed. The effects of geometric parameters and surface tension are discussed in detail. The mechanism of heat transfer enhancement is revealed. The remainder of this paper is organized as follows. The numerical method is introduced briefly in Section 2. The validation is described in Section 3. Detailed results are discussed in Section 4 and concluding remarks are presented in Section 5.

2. Numerical method

2.1. The pseudo-potential lattice Boltzmann model for two-phase flows

Here the pseudo-potential LBM [14] in two dimensions for a single-component two-phase system is adopted. The single relaxation time lattice Boltzmann equation with the Bhatnagar-Gross-Krook (BGK) collision term is used to describe the evolution of the density distribution function, which can be expressed as follows:

$$f_a(\mathbf{x}+\mathbf{e}_a\Delta t, t+\Delta t) = f_a(\mathbf{x},t) - \frac{\Delta t}{\tau}\left[f_a(\mathbf{x},t) - f_a^{eq}(\mathbf{x},t)\right] + \Delta f_a(\mathbf{x},t), \tag{1}$$

where $f_a(\mathbf{x},t)$ is the density distribution function in the ath velocity direction at position $\mathbf{x}$ and time t, and τ is the relaxation time related to the kinematic viscosity as $\nu = c_s^2(\tau - 0.5\Delta t)$. The equilibrium distribution function $f_a^{eq}(\mathbf{x},t)$ can be calculated as

$$f_a^{eq}(\mathbf{x},t) = w_a\rho\left[1 + \frac{\mathbf{e}_a\cdot\mathbf{u}}{c_s^2} + \frac{(\mathbf{e}_a\cdot\mathbf{u})^2}{2c_s^4} - \frac{\mathbf{u}^2}{2c_s^2}\right], \tag{2}$$

where w_a are the weighting coefficients and c_s is the lattice sound speed. In present study, the D2Q9 model is adopted. For this model, $w_a = 4/9$ for $a = 0, w_a = 1/9$ for $a = 1,2,3,4$, and $w_a = 1/36$ for $a = 5,6,7,8$. $c_s = c/\sqrt{3}$, where $c = \Delta x/\Delta t$ is the ratio of lattice spacing Δx and time step Δt. Lattice unit is adopted in this paper. The discrete velocity vectors are given by

$$\mathbf{e}_a = \begin{cases} (0,0), & a = 0 \\ \left[cos\left(\frac{a-1}{2}\pi\right), sin\left(\frac{a-1}{2}\pi\right)\right]c, & a = 1,2,3,4 \\ \left[cos\left(\frac{a-5}{2}\pi + \frac{1}{4}\pi\right), sin\left(\frac{a-5}{2}\pi + \frac{1}{4}\pi\right)\right]\sqrt{2}c, & a = 5,6,7,8. \end{cases} \tag{3}$$

In Eq. (2), ρ is the density of fluid and $\mathbf{u}$ is the velocity. They are obtained by

$$\rho = \sum_a f_a, \quad \rho\mathbf{u} = \sum_a \mathbf{e}_a f_a. \tag{4}$$

The actual whole fluid velocity $\mathbf{v}$ is defined as [29,30]:

$$\mathbf{v} = \mathbf{u} + \frac{\mathbf{F}}{2\rho}, \tag{5}$$

where $\mathbf{F}$ is the body force acting on the fluid nodes. In Eq. (1), the exact difference method [31] is used to implement the body force term. $\Delta f_a(\mathbf{x},t)$ is given by

$$\Delta f_a(\mathbf{x},t) = f_a^{eq}(\rho, \mathbf{u}+\Delta\mathbf{u}) - f_a^{eq}(\rho,\mathbf{u}), \tag{6}$$

where $\Delta\mathbf{u} = \mathbf{F}\Delta t/\rho$ is the velocity change due to the action of body force, and the force is given by

$$\mathbf{F}(\mathbf{x}) = \mathbf{F}_{int}(\mathbf{x}) + \mathbf{F}_g(\mathbf{x}) + \mathbf{F}_{ads}(\mathbf{x}), \tag{7}$$

which includes the inter-particle interaction force $\mathbf{F}_{int}$, the gravitational force $\mathbf{F}_g$, and the adhesion force between liquid/vapor phase and solid phase $\mathbf{F}_{ads}$.

For the inter-particle interaction force, in order to improve numerical accuracy, the scheme presented by Gong and Cheng [18] is adopted, which is defined as

$$\begin{aligned}\mathbf{F}_{int}(\mathbf{x}) = &-\beta\psi(\mathbf{x})\sum_{\mathbf{x}'} G(\mathbf{x},\mathbf{x}')\psi(\mathbf{x}')(\mathbf{x}'-\mathbf{x}) \\ &- \frac{1-\beta}{2}\sum_{\mathbf{x}'} G(\mathbf{x},\mathbf{x}')\psi^2(\mathbf{x}')(\mathbf{x}'-\mathbf{x}),\end{aligned} \tag{8}$$

where ψ is a effective number density [14], β is a weighting coefficient related to the equation of state [18], and $G(\mathbf{x},\mathbf{x}')$ is a function that reflects the interaction strength between two neighboring fluid particles. For D2Q9 scheme, $G(\mathbf{x},\mathbf{x}')$ is given by

$$G(\mathbf{x},\mathbf{x}') = \begin{cases} G, & |\mathbf{x}'-\mathbf{x}| = 1 \\ G/4, & |\mathbf{x}'-\mathbf{x}| = \sqrt{2}, \\ 0, & |\mathbf{x}'-\mathbf{x}| = 0 \end{cases} \tag{9}$$

where G is a parameter that controls the strength of the interparticle interaction force of two nearest neighbors. The effective number density ψ is expressed as $\psi(\mathbf{x}) = \sqrt{2(p - c_s^2\rho)/c_s^2 G}$ according to the Yuan and Schaefer [32]. In this study, a modified form of effective number density is used, which is given by [33]

$$\psi(\mathbf{x}) = \sqrt{\frac{2(\kappa p - c_s^2\rho)}{c_s^2 G}}. \tag{10}$$

Using this formula, a nonideal equation of state could be incorporated into the pseudo-potential LBM. It can be seen that the difference from the original expression of effective number density is that a parameter κ is taken into account in Eq. (10). The surface tension can be adjusted through changing the valve of κ. The Peng-Robinson (P-R) equation of state is used in present work, which is given by

$$p = \frac{\rho RT}{1 - b\rho} - \frac{a\rho^2\alpha(T)}{1 + 2b\rho - b^2\rho^2}, \tag{11}$$

where

$$\alpha(T) = \left[1 + (0.37464 + 1.54226\omega - 0.26992\omega^2)\left(1 - \sqrt{T/T_c}\right)\right]^2$$

with the acentric factor ω and R is the gas constant. The critical properties for the P-R equation of state, such as p_c, T_c can be obtained by setting the first and second derivatives of pressure with respect to density to be zero. Then a and b can be yield as functions of p_c and T_c, i.e., $a = 0.45724(RT_c)^2/p_c$ and $b = 0.0778RT_c/p_c$. For the P-R equation of state, the weighting coefficient β is chosen as $\beta = 1.16$ according to Ref. [18].

For the gravitational force, the form suggested by Bunner and Tryggvason [34] is adopted, which is given by

$$\mathbf{F}_g(\mathbf{x}) = [\rho(\mathbf{x}) - \rho_{ave}] \cdot \mathbf{g}, \tag{12}$$

where ρ_{ave} is the average density of the whole fluid domain and $\mathbf{g}$ is the gravitational acceleration.

The adhesion force between liquid/vapor phase and solid phase relating the wettability of solid wall is calculated by the following equation [13,35]:

$$\mathbf{F}_{ads} = -G_s\psi(\mathbf{x})\sum_a w_a s(\mathbf{x} + \mathbf{e}_a\Delta t) \cdot \mathbf{e}_a. \tag{13}$$

Here $s(\mathbf{x} + \mathbf{e}_a\Delta t)$ is an indicator function that is equal to 1 or 0 for a solid or a fluid domain node, respectively. The desired contact angle can be obtained through changing the fluid-solid interaction strength G_s[13,35].

2.2. Energy equation model

Now we turn to the energy equation. Neglecting viscous heat dissipation, the entropy balance equation is given by [36]

$$\rho T\frac{ds}{dt} = \nabla \cdot (\lambda\nabla T), \tag{14}$$

where s is the entropy and λ is the thermal conductivity. Using the thermodynamic relation given by

$$Tds = c_v dT + T\left(\frac{\partial p}{\partial T}\right)_v dv = c_v dT - T\frac{1}{\rho^2}\left(\frac{\partial p}{\partial T}\right)_\rho d\rho, \tag{15}$$

Eq. (14) can be rewritten as

$$\frac{dT}{dt} = \frac{1}{\rho c_v}\nabla \cdot (\lambda\nabla T) + \frac{T}{\rho^2 c_v}\left(\frac{\partial p}{\partial T}\right)_\rho \frac{d\rho}{dt}, \tag{16}$$

where c_v is the specific heat at constant volume and v is the specific volume. Substituting the mass conservation equation $\partial\rho/\partial t + \nabla \cdot (\rho\mathbf{v}) = 0$ into Eq. (16) and using the relation $dT/dt = \partial T/\partial t + \mathbf{v} \cdot \nabla T$, we have [22]

$$\frac{\partial T}{\partial t} = -\mathbf{v} \cdot \nabla T + \frac{1}{\rho c_v}\nabla \cdot (\lambda\nabla T) - \frac{T}{\rho c_v}\left(\frac{\partial p}{\partial_T}\right)_\rho \nabla \cdot \mathbf{v}. \tag{17}$$

For description convenience, the right-hand side of above equation is referred to as $M(T)$, which is a function of temperature. The second-order Runge-Kutta scheme is directly applied to solve Eq. (17):

$$T(\mathbf{x}, t + \Delta t) = T(\mathbf{x}, t) + \frac{\Delta t}{2}(h_1 + h_2), \tag{18}$$

where h_1 and h_2 represent

$$h_1 = M[T(\mathbf{x}, t)], \quad h_2 = M\left[T(\mathbf{x}, t) + \frac{\Delta t}{2}h_1\right]. \tag{19}$$

For the first derivative and second derivative in Eq. (17), the second-order central discretization is adopted,

$$\frac{\partial\phi}{\partial x_i} = \frac{1}{2c_s^2\Delta t}\sum_a w_a\mathbf{e}_a \cdot \mathbf{i}[\phi(\mathbf{x} + \mathbf{e}_a\Delta t) - \phi(\mathbf{x} - \mathbf{e}_a\Delta t)], \tag{20}$$

$$\frac{\partial^2\phi}{\partial x_i\partial x_i} = \frac{1}{c_s^2(\Delta t)^2}\sum_a w_a[\phi(\mathbf{x} + \mathbf{e}_a\Delta t) - 2\phi(\mathbf{x}) + \phi(\mathbf{x} - \mathbf{e}_a\Delta t)], \tag{21}$$

where $\mathbf{i}$ is the unit vector pointing along the i-coordinate axis and ϕ represents a physical variable, such as v, T.

2.3. Fluid-solid conjugate heat transfer interface treatment

As mentioned above, a two-dimensional fluid-solid conjugate heat transfer problem is considered in this work. The schematic diagram for conjugate heat transfer condition is shown in Fig. 1. The fluid region and solid region are represented by Ω_f and Ω_s, respectively. The fluid-solid interface is denoted by Γ. Usually, the fluid and solid materials have different physical properties, such as density, thermal conductivity, and specific heat.

The conjugate heat transfer interface condition is given by temperature continuity equation and normal heat flux continuity equation:

$$T(\mathbf{x}_i)|_{\Omega_f} = T(\mathbf{x}_i)|_{\Omega_s}, \tag{22}$$

$$-\lambda_f\frac{\partial T}{\partial \mathbf{n}}|_{\mathbf{x}_i,\Omega_f} = -\lambda_s\frac{\partial T}{\partial \mathbf{n}}|_{\mathbf{x}_i,\Omega_s}, \tag{23}$$

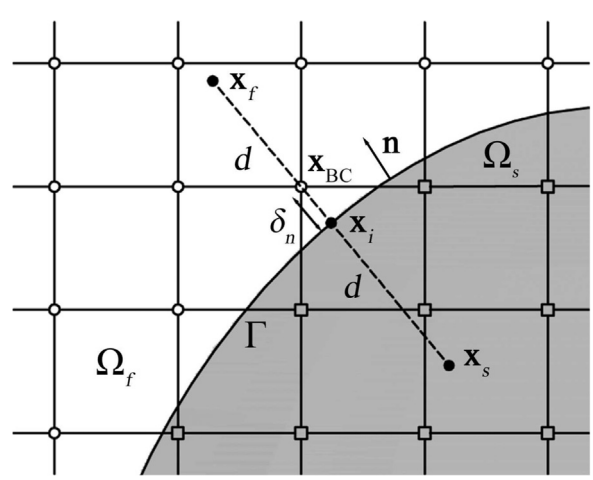

Fig. 1. Schematic diagram of fluid-solid conjugate heat transfer problem, where Ω_f, Ω_s, and Γ denote fluid region, solid region, and fluid-solid interface, respectively, $\mathbf{x}_{BC}$ and $\mathbf{x}_i$ are boundary node and interface point, respectively and δ_n is the distance of them.

where λ_f and λ_s denote thermal conductivity of fluid and solid, respectively, $\mathbf{n}$ is the unit outward normal vector on Γ. In some previous studies [22,37], the energy equation was solved by the LBM, and the conjugate heat transfer condition was implemented through calculating the distribution function for the temperature near the fluid-solid interface. Here, Eq. (22) and Eq. (23) are directly ensured in our finite-difference scheme for the energy equation.

Eq. (23) is discretized using a semi-second-order approximation as follows [38]:

$$-\lambda_f \frac{T(\mathbf{x}_f) - T(\mathbf{x}_i)}{d} = -\lambda_s \frac{T(\mathbf{x}_i) - T(\mathbf{x}_s)}{d}. \tag{24}$$

$\mathbf{x}_s$ and $\mathbf{x}_f$ may not lie on the nodes in somewhere. Therefore bilinear interpolation is used to calculate the temperatures in these locations. The distance d is chosen to be $d = 1.5$. Once the temperatures on $\mathbf{x}_s$ and $\mathbf{x}_f$ are got, the temperature at the interface is given by

$$T(\mathbf{x}_i) = \frac{\lambda_s T(\mathbf{x}_s) + \lambda_f T(\mathbf{x}_f)}{\lambda_s + \lambda_f}. \tag{25}$$

Then the temperatures on the boundary nodes $\mathbf{x}_{BC}$ can be calculated by

$$T(\mathbf{x}_{BC}) = T(\mathbf{x}_i) + \frac{\delta_n}{d}\left[T(\mathbf{x}_f) - T(\mathbf{x}_i)\right]. \tag{26}$$

For the boundary nodes that lie on the Ω_s, the same procedure is applied.

In summary, when the velocity field at $t + \Delta t$ is known according Eq. (5), we can get the distribution of temperature at nodes away from the boundary through solving Eq. (17), and those at the boundary nodes by using Eq. (24)–(26). In this way, the entire temperature filed at $t + \Delta t$ is obtained.

3. Numerical validations

3.1. Coexistence curves

In order to validate the present pseudo-potential LB model, first the coexistence curves of P-R equation of state are obtained from LBM simulations, and then compared with analytical solutions. Test cases of a droplet immersed in vapor in the absence of gravity are simulated. In these simulations, $\tau = 1.0, a = 2/98, b = 2/21$ and $R = 1$. The computational domain is 300×300 and periodic boundary condition is applied on all boundaries. A circular area in the center of the domain is initialized as liquid area (higher density) while the other region is initialized as vapor area (lower density). After the simulations reach the equilibrium state, the equilibrium densities of the liquid and vapor are obtained. Through simulating many cases at different T, and measuring the equilibrium densities, the coexistence curves can be obtained. Three curves for $\kappa = 1.0, \kappa = 3.0$, and $\kappa = 5.0$ are plotted in Fig. 2(a). The analytical coexistence curve obtained from the Maxwell construction [13] is also shown in Fig. 2(a) for comparison. It is seen that three coexistence curves from LBM simulations are all approximately consistent with the analytical one. Thermodynamic consistency of present model is verified. It is worth noting that the surface tension varies for different κ at the same temperature and there are small discrepancies for the equilibrium density of vapor phase for $\kappa = 1.0$ and $\kappa = 5.0$ (see Fig. 2(a)).

For above simulations, after the equilibrium state reaches, the surface tension σ can be calculated numerically using the two-dimension Laplace's law: $\Delta p = \sigma/R$, where Δp is the pressure difference across the two-phase interface and R is the radius of droplet. To obtain a more accurate σ, serval cases with different initial droplet sizes are simulated and discrete points in the $\Delta p - 1/R$ plot are obtained. The slope of the fitted line for these points is σ. From Fig. 2(b) it is seen that for $\kappa = 1.0, \kappa = 3.0$, and $\kappa = 5.0$ at $T = 0.85T_c$, the surface tension are $0.109, 0.065$, and 0.051, respectively. Hence, the surface tension can be adjusted through changing the coefficient κ.

3.2. Bubble nucleation and growth from a V-shaped cavity

To further validate our numerical method, a problem of bubble heterogeneous nucleation from a V-shaped cavity is studied, which includes phase change and conjugate heat transfer boundary condition.

The computational domain is a two-dimensional rectangular with a 400×500 mesh. The solid substrate with a V-shaped cavity is located at the bottom of domain (see Fig. 3(a)). γ is the angle and L_d is the vertical depth of the cavity. Constant temperature boundary condition with $T_b = T_s + \Delta T$ is specified on the bottom of the substrate, where T_s is the saturated temperature. Periodic boundary condition is imposed on the left and right boundaries. Constant pressure boundary condition is applied on the top of domain [39]. The halfway bounce-back scheme for nonslip boundary condition and conjugate heat transfer condition are applied at the fluid-solid interface. Initially, a fan-shaped small area in the base of cavity is set to be a small nucleus occupied by saturated vapor, and the other region of fluid domain is filled with saturated liquid at $T_s = 0.875T_c$. The initial temperature of the computational domain is set to be T_s. The saturated densities of liquid and vapor at $T_s = 0.875T_c$ are $\rho_l = 6.29$ and $\rho_v = 0.44$, where subscripts "l" and "v" denote liquid and vapor, respectively. Other properties is given in Table 1. The surface tension is chosen to be $\sigma = 0.116\,(\kappa = 1)$ and the static contact angle is set to be

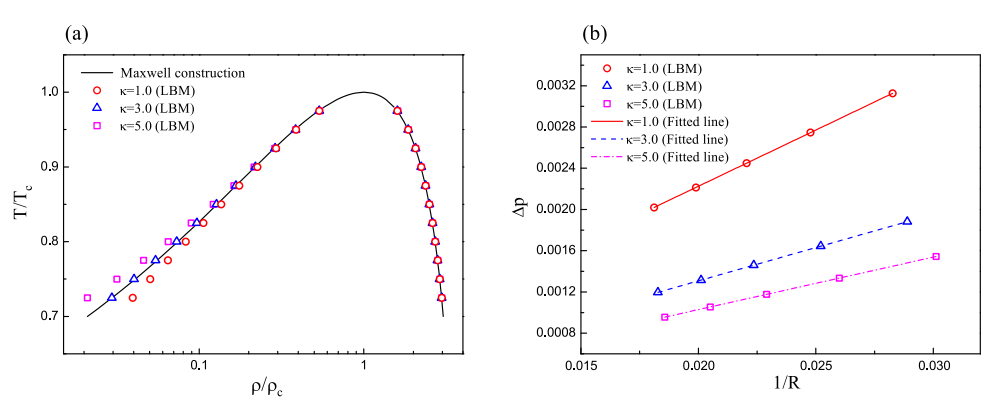

Fig. 2. (a) Comparison of the coexistence curves obtained from present model for different κ and analytical solution. (b) Determination of the surface tension using the Laplace's law for different κ.

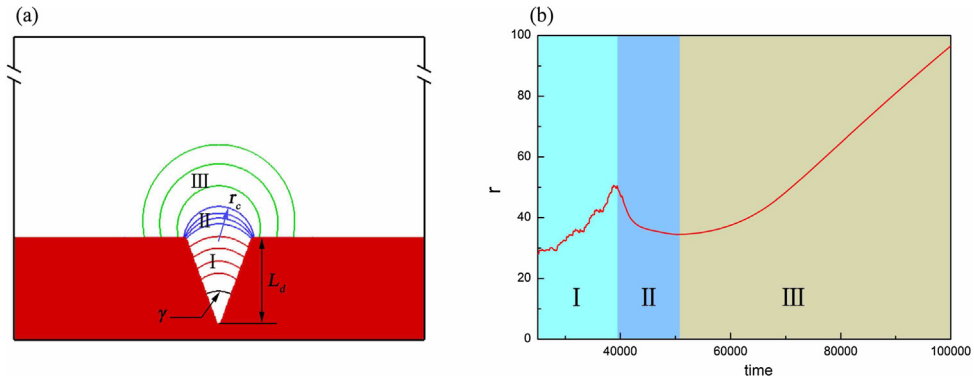

Fig. 3. (a) Bubble heterogeneous nucleation process from a *V*-shaped cavity with $\gamma = 40^\circ$. $r_c = L_d \tan(\frac{\gamma}{2})$ for a hydrophilic wall is the critical radius when the bubble reaches the mouth of the cavity. (b) The radius of bubble as a function of time during bubble heterogeneous nucleation with $\gamma = 40^\circ$.

Table 1
Physical properties adopted in the simulations (lattice units).

	Liquid	Vapor	Solid
Density(ρ)	6.29	0.44	78.6
Kinetic viscosity(ν)	0.10	0.17	–
Specific heat(c_v, c_p)	8.0	6.0	4.5
Thermal conductivity(λ)	22.65	1.21	226.5

$\theta = 71.4^\circ$ through specifying $G_s = -1.68$ in Eq. (13). For the parameters in the EOS, we set $a = 2/49, b = 2/21$, and $R = 1$. The specific latent heat is $h = 0.3622$, which is calculated by the theory presented in the Appendix of [40]. The effect of gravity is not considered, i.e., $\mathbf{g} = (0, 0)$.

Usually, there are three stages listed in the following for the bubble heterogeneous nucleation from a *V*-shaped cavity [41]. (I) The bubble grows inside the cavity and radius increases. (II) The bubble reaches the mouth of the cavity and the contact line is almost pinned at the mouth. The radius decreases gradually due to increase of the bubble volume. (III) The bubble further continuously grows on the platform of substrate and radius increases again.

In our LBM simulation, to allow the system reach an equilibrium state, the temperature of the whole system is set to be T_s for the initial 20,000 time steps. At $t = 20,000$, the temperature of the bottom of the substrate is raised to $T = T_b$. Because $T_b > T_s$, heat would be conducted from the bottom of the substrate to the fluid-solid interface. At $t \approx 25,000$, the fluid-solid interface becomes hot enough and the initial bubble begins to grow. Fig. 3 (a) shows the bubble growth process and Fig. 3(b) shows bubble radius r as a function of time in the LBM simulation. It is seen that in stage I ($25,000 < t < 40,000$), r increases continuously due to the bubble growth. In stage II ($40,000 < t < 50,000$), r decreases to a valley r_c and in stage III ($t > 50,000$), it increases again. Hence, three stages of bubble nucleation from a cavity [41] have been qualitatively reproduced using the present numerical method.

For bubble growth in two-dimensional cases, the relationship between superheat of liquid film ΔT_s and critical radius of bubble r_c is [42]

$$\Delta T_s = \frac{\sigma T_s}{h \rho_v r_c}, \tag{27}$$

where $r_c = L_d \tan(\frac{\gamma}{2})$ for a hydrophilic wall. r_c is the minimum of bubble radius when the bubble grows at the mouth of the cavity (see Fig. 3(a) or $t \approx 50,000$ in Fig. 3(b)). Only the superheat of the liquid near the top of the bubble at $r = r_c$ is greater than ΔT_s, can the bubble continue to grow. Otherwise the bubble will gradually collapse. For a case with a specific r_c (or γ), several simulations with different T_b are performed to obtain the critical superheat ΔT_s. For example, if in the simulation with $T_b = T_s + \Delta T - \delta$ the bubble growth ceases while when $T_b = T_s + \Delta T + \delta$, the bubble continuously grows, and δ is a small value, we confirm the critical superheat of the liquid film can be measured from the latter case with $\Delta T_s = T_o - T_s$, where T_o is the temperature of the liquid near the top of the bubble.

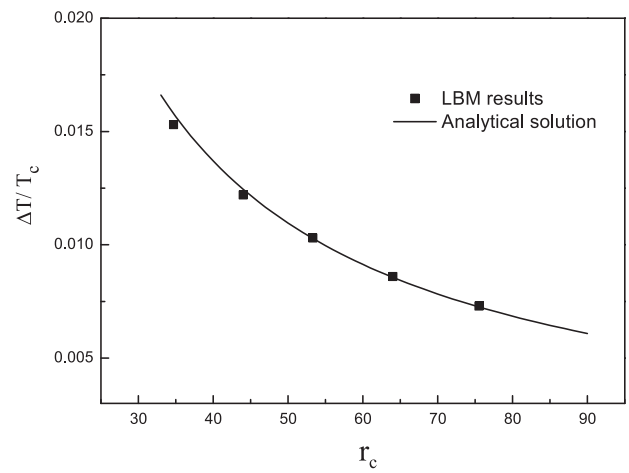

Fig. 4. The critical superheat ΔT_s as a function of the critical radius r_c.

Changing the angle of cavity γ, we obtained cases with different r_c. Through numerous simulations, ΔT_s as a function of r_c can be obtained. Fig. 4 shows the comparison between the LBM results and the analytical one. It is seen that the LBM results are almost consistent with the analytical solution given by Eq. (27).

From the above validations, it is seen that the present thermal LB model is able to capture the dynamic and thermodynamic characteristics of boiling heat transfer on structured surfaces.

4. Results and discussions

In this section, pool boiling heat transfer on a typical structured surface with columns is studied. The two dimensional computational mesh size is $L_x \times L_y = 840 \times 1000$. The schematic diagram is shown in Fig. 5. The solid substrate with columns is located at the bottom of the domain, which is also shown in Fig. 5. These columns are characterized by width W and height H with gap spacing

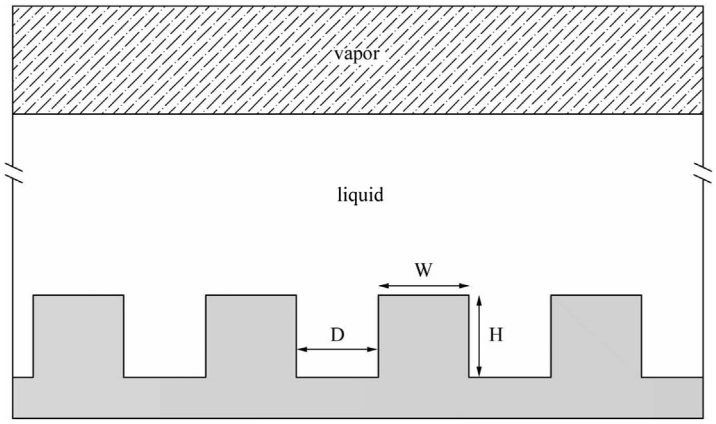

Fig. 5. Schematic diagram of structured surface with columns.

D. In our simulations, the effects of the geometrical parameters are explored.

Initially, the fluid region is occupied by saturated liquid at $y < 0.7L_y$ and its saturated vapor at $y > 0.7L_y$. The initial densities of liquid and vapor are $\rho_l = 6.63$ and $\rho_v = 0.35$ at $T_s = 0.85T_c$. The nonslip boundary condition and the conjugate heat transfer condition are applied at fluid-solid interface. The nonslip condition is also imposed on the upper boundary of the computational domain. Periodic boundary condition is imposed on the left and right boundaries. The kinematic viscosity and specific heat are also listed in Table 1. Thermal conductivities for liquid, vapor, and solid are $\lambda_l = 2.652, \lambda_v = 0.28$, and $\lambda_s = 265.2$, respectively. The static contact angle is chosen to be $\theta = 74.5^\circ$ and $a = 2/98, b = 2/21, R = 1$. The specific latent heat is $h = 0.1956$. If not specified, The gravity is chosen to be $\mathbf{g} = (0, -0.00005)$.

In these simulations, the characteristic length, velocity and time are chosen as [7,25]

$$l_0 = \sqrt{\frac{\sigma}{g(\rho_l - \rho_v)}}, \quad u_0 = \sqrt{gl_0}, \; t_0 = l_0/u_0. \tag{28}$$

The nondimensional parameters involved in this problem are: the capillary number Ca and the normalized geometrical parameters $\overline{\zeta}$

$$Ca = \frac{\rho_l v_l u_0}{\sigma}, \quad \overline{\zeta} = \frac{\zeta}{l_0}, \tag{29}$$

where ζ may represent D, W, or H.

The transient spatial-averaged heat flux $Q'(t)$ is defined as

$$Q'(t) = -\frac{\lambda_s}{L_x}\int_0^{L_x} \frac{\partial T}{\partial y}|_{y=0} dx. \tag{30}$$

The local temperature gradient at the bottom of substrate is calculated by a biased second-order finite-difference scheme

$$\frac{\partial T}{\partial y}|_{y=0} = \frac{4T|_{y=1} - T|_{y=2} - 3T|_{y=0}}{2\Delta y}, \tag{31}$$

where Δy is the lattice spacing.

Supposing when $t \in (t_1, t_2), Q'(t)$ is almost steady, the temporal averaged heat flux can be calculated as

$$Q'' = \frac{1}{t_2 - t_1}\int_{t_1}^{t_2} Q'(t)dt. \tag{32}$$

4.1. Boiling phenomena

In our numerical simulations, three boiling regimes have been achieved on structured surfaces with columns, i.e., nucleate boiling, transition boiling, and film boiling. Snapshots of the former two boiling processes are shown in Fig. 6. When the substrate temperature is low, the nucleate boiling occurs (Fig. 6(a)), most bubbles generate at the feet of columns while some bubbles may generate on the middle of the channel bottom. The latter bubbles will move to the feet of the columns quickly and merge with the former bubbles. Then, as the liquid surrounding the bubbles further evaporates, the bubbles grow in the feet and rise along the sidewalls of the columns. The bubble detachments from the feet may occur when the bubbles grow large enough. The detached bubbles continue to grow and rise along the sidewalls due to buoyancy. Meanwhile, they leave small nucleuses at the feet for the next bubble generation cycle. When the bubbles reach the top of the columns, the second detachments occur. The bubbles would completely leave the solid substrate and are immersed into the liquid.

As the temperature of the substrate increases, the transition boiling is observed (Fig. 6(b)). In this regime, the number of bubbles is significantly reduced. For example, the leftmost subfigure in Fig. 6(b) shows that there are always vapor columns on the sidewalls of the columns and few bubbles depart at the top of the columns. It is also observed that some small bubbles may generate on the middle of the channel bottom and move to the feet of the columns and coalesce with the vapor columns.

When the substrate temperature is high enough, boiling will be in the film boiling regime. The solid is completely covered by a layer of vapor film. Few bubbles detach from the top of the columns. It is noted that heat transfer performance becomes poorer in the transition and film boiling regimes.

Compared to situation of the plain surface, the heated surface area of the columnar structure surface A becomes larger, which is key to the heat transfer enhancement of the surface. On the other hand, the presence of columnar structure results in a different flow field from that of the plain surface. Typical flow field in nucleate boiling regime is shown in Fig. 7. It is a zoom-in view of the flow filed at $t^* = 128.8$ in Fig. 6(a). The flow field differs from that of the plain surface in the following two aspects. First, there is the convection in the channel between the columns. The cold liquid would be quickly replenished into the channel and heated to evaporate. This feature may enhance the heat transfer. Second, when a bubble rises along the sidewall of the column, there is only one convective vortex on one side of the bubble due to the presence of the column on the other side. Only one convective vortex may be not good because usually two convective vortexes on both sides of the bubble in the case of the plain surface is believed to be more helpful for heat transfer. Therefore, we have to further evaluate different effects on overall performance of heat transfer enhancement of the structured surfaces.

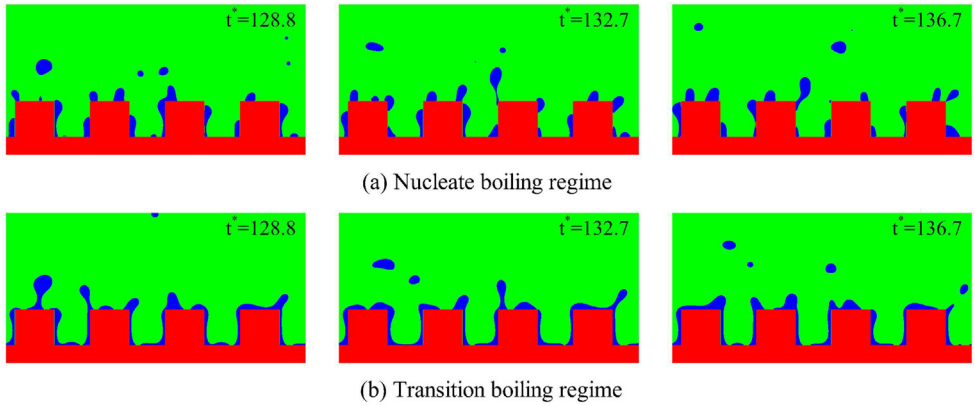

Fig. 6. Snapshots of boiling processes in (a) nucleate boiling regime and (b) transition boiling regime, $\overline{H} = 7.85, \overline{W} = 8.63$, and $\overline{D} = 7.85$.

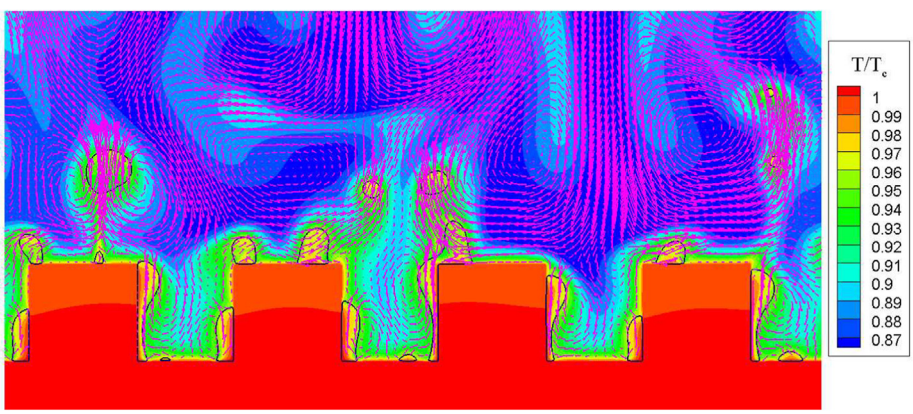

Fig. 7. Velocity field and temperature distribution at $t^* = 128.8$ in nucleate boiling with $\overline{H} = 7.85, \overline{W} = 8.63$, and $\overline{D} = 7.85$, where black solid lines represent bubbles.

4.2. Effect of geometrical parameters

Geometrical parameters affect much on the boiling heat transfer of columnar structure surfaces [3]. Here, we would like to explore the inherent mechanisms. Simulations with different geometrical parameters are performed (see Table 2). For each typical geometry, several cases with different T_b ($T_b = T_s + \Delta T$) are simulated and the whole boiling curve for the geometry can be obtained. In boiling curve, superheated is defined by $\Delta T_i = T_i - T_s$, where T_i is the average temperature at the fluid-solid interface. In fact, in present study, the substrate is not very thick and the thermal conductivity of the solid is much larger than the liquid. Therefore, ΔT_i is approximately equal to ΔT. In the following part, the effects of column height ($\overline{H}$), width ($\overline{W}$) and gap spacing ($\overline{D}$) are studied, respectively. In this part, the capillary number is fixed to be $Ca = 0.3281$.

4.2.1. Effect of column height $\overline{H}$

Fig. 8(a) shows the boiling curves of three columnar structure surfaces with different $\overline{H}$. The boiling curve of the plain surface is also presented for comparison. It is seen that Q'' of three columnar structure surfaces are all higher than that of the plain surface. The higher the height $\overline{H}$, the more prominent the heat transfer enhancement. It is consistent with the experimental results [3]. Besides, a larger CHF is obtained at a higher $\overline{H}$. Three boiling regimes similar to those on a plain surface are confirmed again here. For example, in Case 2, when $\Delta T_i/T_c \in [0.12, 0.20]$, the nucleate boiling happens. At larger $\overline{H}, \Delta T_i/T_c$ of the CHF point also increases, i.e., the boiling mode transition would occur at a higher superheat when $\overline{H}$ is large.

The heat transfer enhancement of the case with a larger $\overline{H}$ is attributed to the increase of the heated surface area A, The increase of A provides more possible nucleation sites and leads to more

Table 2
Geometrical parameters and heat flux increase Q''_c/Q''_p at $\Delta T_i/T_c \approx 0.16$ for different cases, where $A_r = A_c/A_p$ is area increase factor. The subscripts "c" and "p" denote the situation of structured surface and plain surface, respectively.

Case	$\overline{H}$	$\overline{W}$	$\overline{D}$	A_r	$Q''_c/Q''_p(\Delta T_i/T_c \approx 0.16)$
1	3.92	8.63	7.85	1.476	1.098
2	7.85	8.63	7.85	1.952	1.420
3	11.77	8.63	7.85	2.429	1.835
4	7.85	5.34	7.85	2.190	1.432
5	7.85	14.13	7.85	1.714	1.338
6	7.85	8.63	4.55	2.190	1.263
7	7.85	8.63	13.34	1.714	1.405

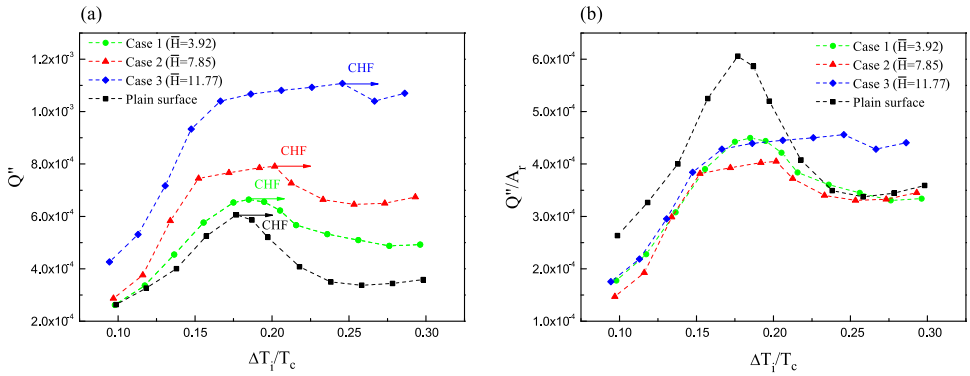

Fig. 8. (a) Boiling curves and (b) normalized boiling curves for cases with different $\overline{H}$.

convection near to the surface. To check whether the heat transfer enhancement is solely due to the increase of the heated area, the heat flux is normalized by the area increase factor A_r. Fig. 8(b) shows the normalized heat flux Q''/A_r as a function of $\Delta T_i/T_c$, i.e., the normalized boiling curves for these cases. It is seen that the curves for different height $\overline{H}$ almost collapse into a single curve in the nucleate boiling regime. Hence, when $\overline{W}$ and $\overline{D}$ are proper (e.g., $\overline{W} \approx \overline{D} = 8$), the heat flux Q'' is approximately solely proportional to A at $\overline{H} \in (4, 12)$ in the nucleate boiling regime.

Data of Cases 1, 2 and 3 in Table 2 also confirms this point. The normalized heights in Cases 1, 2 and 3 are 3.92, 7.85, and 11.77, respectively. Compared to Case 1, A of Cases 2 and 3 increases $\frac{1.952-1.476}{1.476} - 1 = 32.2\%$, $\frac{2.429-1.476}{1.476} - 1 = 64.6\%$, respectively. At $\Delta T_i/T_c \approx 0.16$, the Q'' increases $\frac{1.420-1.098}{1.098} - 1 = 29.3\%$ and $\frac{1.835-1.098}{1.098} - 1 = 67.1\%$, respectively. Here $\Delta T_i/T_c \approx 0.16$ is chosen because it's a typical temperature in the nucleate boiling regime. The increase of Q'' is approximately proportional to the increase of A.

It is also seen from Fig. 8(b) that Q''/A_r for the structured surfaces is smaller than that for the plain surface in the nucleate boiling regime. Q''/A_r is usually relevant to the average convection strength. Hence, the average convection strength near the structured surface is not as strong as that near the plain surface.

4.2.2. Effect of column width $\overline{W}$

In this small section, we would like to discuss the effect of column width $\overline{W}$. Reducing $\overline{W}$ means an increase of the area A because it allows more columns on the substrate. Cases 5, 2 and 4 in Table 2 show that when $\overline{H} = \overline{D} = 7.85$ is fixed, their $\overline{W}$ are 14.13, 8.63, and 5.34, respectively. Compared to Case 5, A of Cases 2 and 4 increases $\frac{1.952-1.714}{1.714} - 1 = 13.9\%$, $\frac{2.190-1.714}{1.714} - 1 = 27.8\%$, respectively. However, the Q'' increases $\frac{1.420-1.338}{1.338} - 1 = 6.1\%$ and $\frac{1.432-1.338}{1.338} - 1 = 7.0\%$, respectively. Hence, at $\Delta T_i/T_c \approx 0.16$ the increase of Q'' is slower than the increase of A.

The effect of $\overline{W}$ on normalized heat flux Q''/A_r is shown in Fig. 9. It is seen that the curves for different height $\overline{W}$ do not collapse into a single curve in the nucleate boiling regime. Besides, Q''/A_r as well as the normalized CHF decreases as $\overline{W}$ decreases. Hence, the increase of heat flux Q'' is slower than the increase of A at $\overline{W} \in (5, 14)$. The fact implies that some unfavorable factors hinder the heat transfer enhancement as $\overline{W}$ is reduced.

Fig. 10 shows the velocity fields of Case 4 ($\overline{W} = 5.34$) and Case 5 ($\overline{W} = 14.13$) at $t^* = 118.87$ with $\Delta T_i/T_c \approx 0.18$. It is seen that more convective liquid is able to contact with the top of columns when $\overline{W}$ is large while more liquid pathways are blocked when $\overline{W}$ is small due to the top wall is mostly covered by bubbles. Hence,

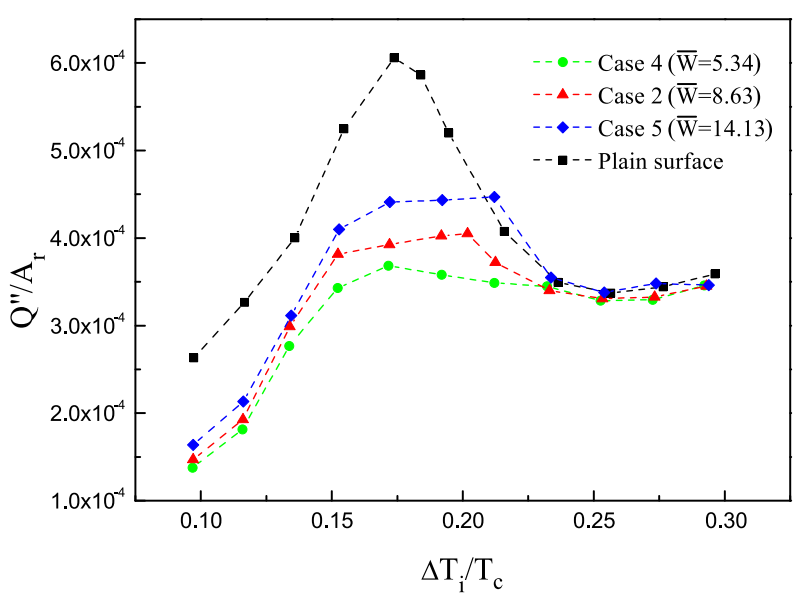

Fig. 9. Normalized boiling curves for the cases with different $\overline{W}$.

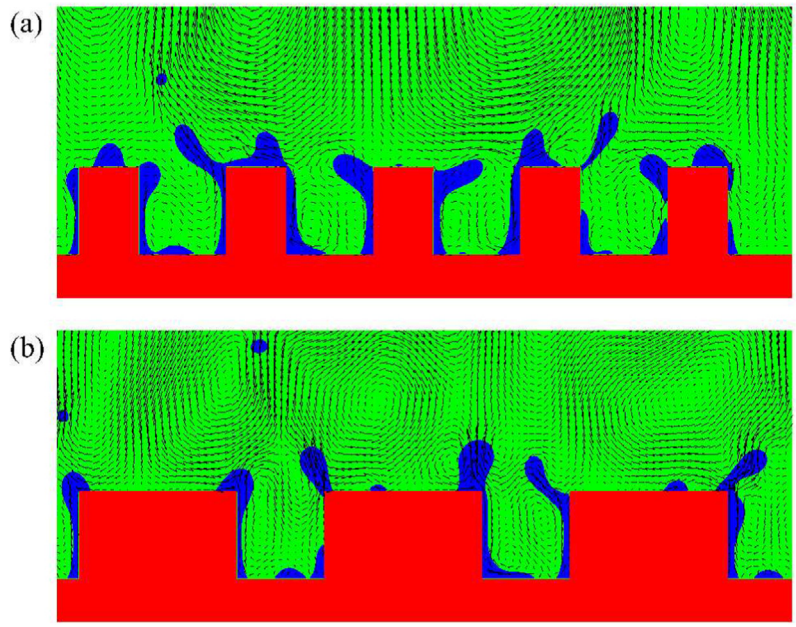

Fig. 10. Velocity field at $t^* = 118.87$ in nucleate boiling at $\Delta T_i/T_c \approx 0.18$ for (a) Case 4 ($\overline{W} = 5.34$) and (b) Case 5 ($\overline{W} = 14.13$).

although the heated area increases, heat transfer enhancement is not so significant as $\overline{W}$ is small.

4.2.3. Effect of column gap spacing $\overline{D}$

Effect of column gap spacing D is discussed in the follows. Reducing $\overline{D}$ also means an increase of surface area A because it allows more columns on the substrate (see Table 2). From the Table it is seen that in Cases 7, 2 and 6 as $\overline{D}$ decreases (i.e., A increases), Q'' at $\Delta T_i/T_c \approx 0.16$ increases first and then decreases. This means that the reduction of $\overline{D}$ may be not advantageous for boiling heat transfer, which even completely eliminates the heat transfer enhancement due to the increase of A.

The effect of $\overline{D}$ on Q''/A_r is shown in Fig. 11. It can be observed that as $\overline{D}$ decreases, Q''/A_r in the nucleate boiling regime and the normalized CHF decrease significantly. This is consistent with the experimental results [3]. The different heat transfer performance is mainly caused by the flow fields at different $\overline{D}$. Large $\overline{D}$ can greatly improve the convection of cold liquid into the channel just like the situation in Fig. 12(c). After entering the channel, the cold liquid is rapidly heated and phase change occurs continuously. When $\overline{D}$ is small, this convection is weakened (Fig. 12(b)) or the channel may be completely filled by coalescent bubbles (Fig. 12(a)). The layer of thicker vapor film covering the solid wall blocks the effective heat transfer. Hence, the flow field of the case with a smaller $\overline{D}$ hinders the heat transfer performance.

To analyse the flow field, supposing the fluid-solid interface is divided into three segments, i.e., channel bottom, column top, and sidewall, the space- and time-averaged heat fluxes at these segments are Q''_{bottom}, Q''_{top}, and $Q''_{sidewall}$, respectively. Their definitions are similar to Eq. (32). These fluxes in Cases 7, 2 and 6 at

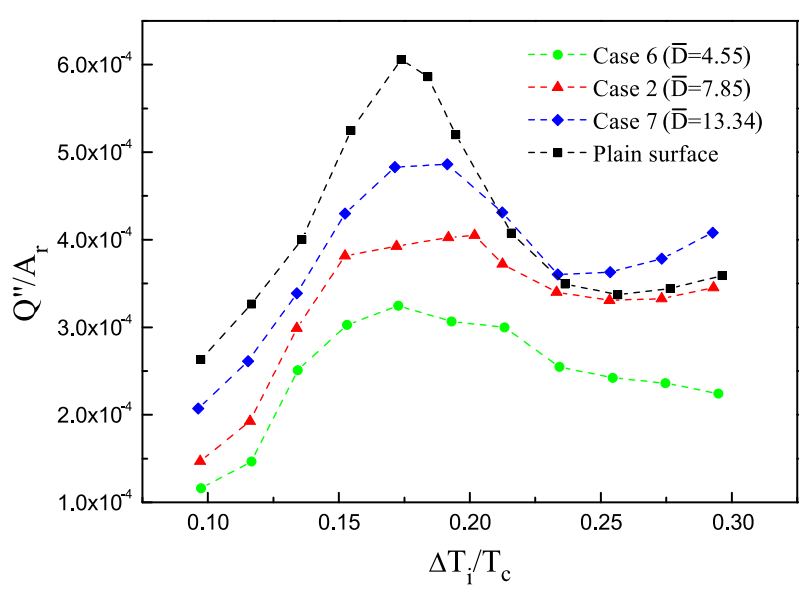

Fig. 11. Normalized boiling curves for the cases with different $\overline{D}$.

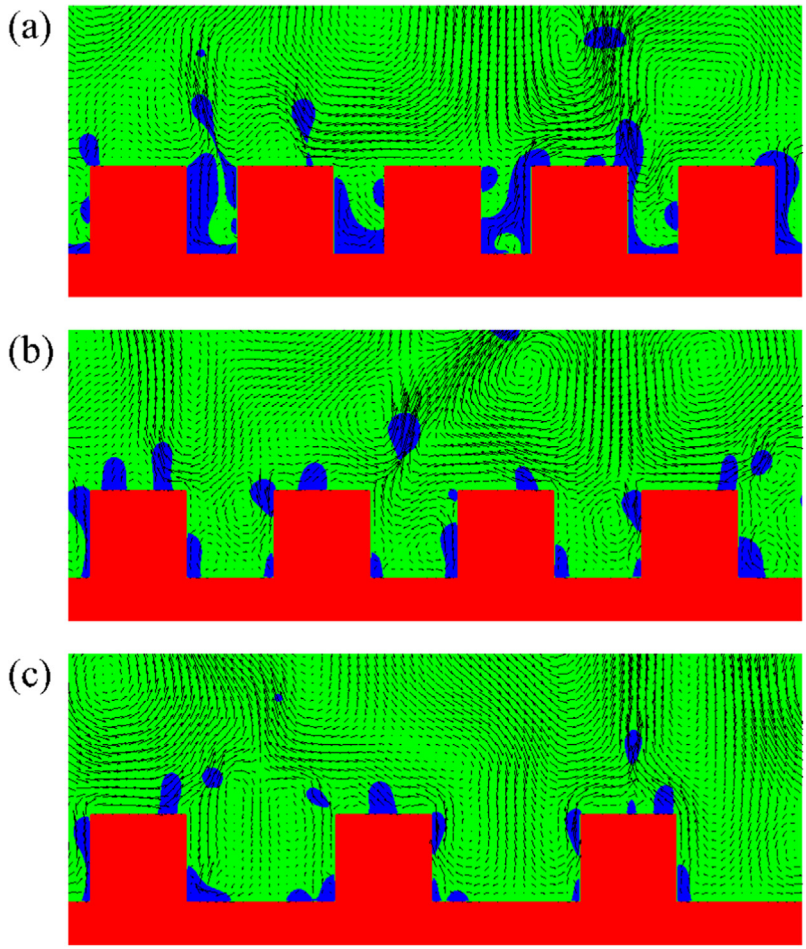

Fig. 12. Velocity field at $t^* = 138.68$ in nucleate boiling at $\Delta T_i/T_c \approx 0.18$ for (a) Case 6 ($\overline{D} = 4.55$) (b) Case 2 ($\overline{D} = 7.85$), and (c) Case 7 ($\overline{D} = 13.34$).

$\Delta T_i/T_c \approx 0.18$ are shown in Fig. 13. It is seen that as $\overline{D}$ decreases, Q''_{top} is substantially unchanged but Q''_{bottom} and $Q''_{sidewall}$ are significantly reduced. This confirms that the convection in channel is hindered due to small $\overline{D}$. Hence, it seems that a small D is not favorable for heat transfer enhancement in our 2D simulations. However, for 3D cases this conclusion may be invalid due to the wicking effect.

4.3. Effect of surface tension σ

Surface tension σ has a great influence on boiling heat transfer by affecting the bubble detachment. The effect of σ on the boiling heat transfer performance is discussed in the following.

Fig. 14 shows the boiling curves for different Ca. It is seen that as Ca increases, Q'' increases in the nucleate boiling regime. Table 3

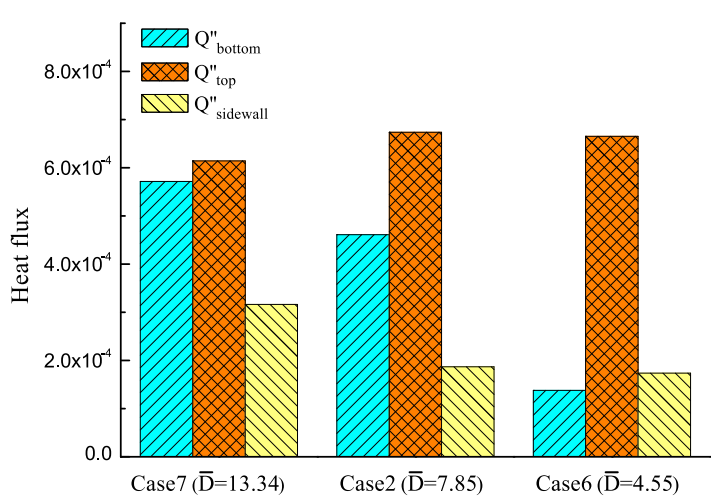

Fig. 13. The space- and time-averaged heat fluxes at three segments of fluid-solid interface for different $\overline{D}$ at $\Delta T_i/T_c \approx 0.18$.

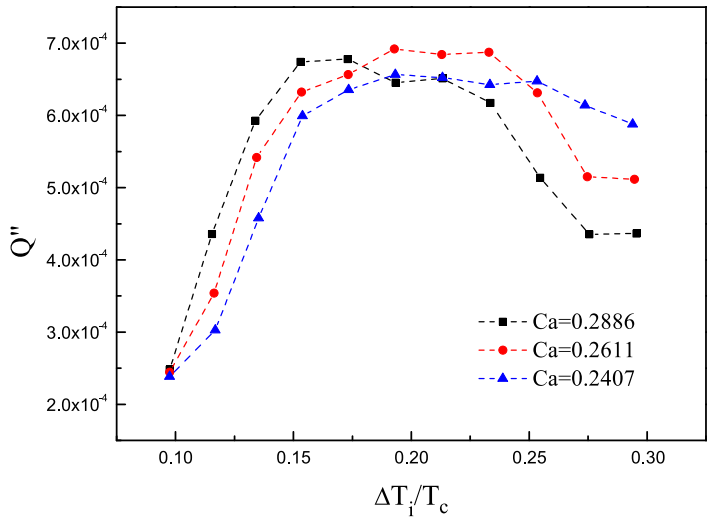

Fig. 14. Boiling curves for the simulation cases with different *Ca*.

Table 3
Heat transfer at different *Ca* with $\Delta T_i/T_c \approx 0.16$ for the structured surface and the plain surface.

	$Ca = 0.2407$	$Ca = 0.2611$	$Ca = 0.2886$
Q''_p	4.42×10^{-4}	5.54×10^{-4}	5.95×10^{-4}
Q''_c	5.99×10^{-4}	6.32×10^{-4}	6.74×10^{-4}
Enhancement ratio η	35.6%	14.0%	13.3%

also shows that Q'' for the structured surface increases with *Ca* at $\Delta T_i/T_c \approx 0.16$. The feature is mainly attributed to the bubble behaviors due to surface tension. Fig. 15 shows the snapshots of nucleate boiling at (a) $Ca = 0.2407$ and (b) $Ca = 0.2886$, corresponding to $\sigma = 0.065$ and $\sigma = 0.051$, respectively. It is seen that the flow pattern is quite different in the two cases. The average bubble size at $Ca = 0.2886$ is significantly larger than that at $Ca = 0.2407$. Larger bubbles at $Ca = 0.2886$ could carry more heat away from the surface, which would enhance the heat transfer.

Actually not only Q'' of the structured surface but also that of the plain surface increases with *Ca* (see Table 3). The enhancement ratio $\eta = \frac{Q''_c}{Q''_p} - 1$ is used to quantify the performance of the structured surface compared to that of the plain surface. Table 3 shows that η decreases with *Ca*. It can be understood in the following way. As shown in Fig. 15, at $Ca = 0.2407$, bubbles move to the platform of the columns and then departure. The channels seem still open and the cold liquid can be convected into the channel easily, which is beneficial to enhance heat transfer. Both the convection in the cases of the structured and plain surfaces are not hindered. The heat transfer enhancement $\eta = 35.6\%$ is purely due to the larger heated area *A* in the case of the structured surface. As *Ca* increases, Fig. 15(b) shows that more vapor may cover the channels. Besides, the path of the convection of the cool liquid may be partially blocked because bubbles depart from the edges of columns. The two factors all hinder the effective heat transfer. While in the case of plain surface, usually the convection is not hindered. Therefore, η becomes smaller than that at small *Ca*.

5. Conclusions

Using a two-dimensional thermal lattice Boltzmann two-phase model, the pool boiling heat transfer enhancement on structured surfaces is investigated. Phase change is controlled by an equation of state automatically and a fluid-solid conjugate heat transfer interface treatment is imposed. Present method is shown to be able to simulate boiling heat transfer on structured surfaces. Boiling heat transfer performance on structured surfaces with columns are studied. The feature size in this work is much larger than capillary length. Compared to a smooth surface, the enhancement of boiling performance is relevant to the surface area augmentation. We summarize the results of the study as follows.

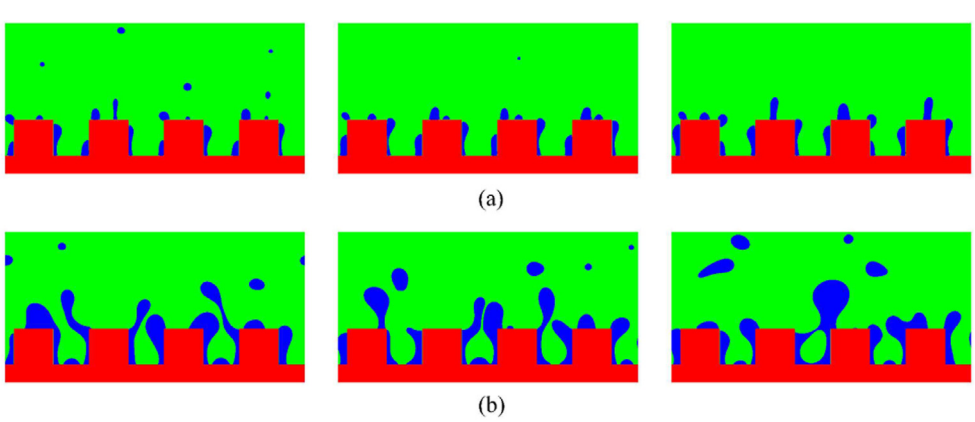

Fig. 15. Snapshots of boiling process in nucleate boiling regime for (a) $Ca = 0.2407$ and (b) $Ca = 0.2886$.

Geometrical parameters have important effects on the boiling heat transfer. When $\overline{W}$ and $\overline{D}$ is proper, increasing $\overline{H}$ enhances the heat transfer solely due to the increase of surface area A.

When $\overline{W}$ is small, it is observed that the top of the columns is mostly covered by bubbles. Under the circumstances, although A increases, heat transfer enhancement is not so significant because less convective liquid is able to contact with the top of columns. When $\overline{D}$ is small, the convection is weakened or the channel may be completely filled by coalescent bubbles. They all hinder the effective heat transfer. Hence, both increasing of $\overline{W}$ and $\overline{D}$ would result in a larger Q''/A_r because the convection in the column top and in the channel is improved, respectively.

Surface tension σ also has a great influence on boiling heat transfer. The average bubble size at larger Ca is significantly larger than that at small Ca. Hence the heat transfer would be enhanced at larger Ca. On the other hand, the enhancement ratio η between the structured and plain surfaces decreases with Ca. At smaller Ca, both the convection in the cases of the structured and plain surfaces are not hindered. The heat transfer enhancement is mainly due to the larger heated area A in the case of the structured surface. As Ca increases, the convection close to the channel may be partially blocked due to the bubbles detachment from the edge of column top. That would hinder the effective heat transfer. While in the case of plain surface, usually the convection is not hindered. Therefore, η is decreased at large Ca.

In general, two factors affect the enhanced heat transfer effect of pool boiling on the structured surfaces: the surface area and convection near the bubble. An optimal enhancement could be achieved when A is as large as possible and meanwhile the convection is not hindered by the bubbles behaviors.

Declaration of Competing Interest

None.

Acknowledgement

Huang is supported by National Natural Science Foundation of China (Grant No. 11472269).

References

[1] H.J. Cho, D.J. Preston, Y. Zhu, E.N. Wang, Nanoengineered materials for liquid–vapour phase-change heat transfer, Nat. Rev. Mater. 2 (2) (2017) 16092.
[2] D. Cooke, S.G. Kandlikar, Pool boiling heat transfer and bubble dynamics over plain and enhanced microchannels, J. Heat Transf. 133 (2011), 052902.
[3] D. Cooke, S.G. Kandlikar, Effect of open microchannel geometry on pool boiling enhancement, Int. J. Heat Mass Transf. 55 (4) (2012) 1004–1013.
[4] J. Wei, L. Guo, H. Honda, Experimental study of boiling phenomena and heat transfer performances of fc-72 over micro-pin-finned silicon chips, Heat Mass Transfer. 41 (8) (2005) 744–755.
[5] K.-H. Chu, R. Enright, E.N. Wang, Structured surfaces for enhanced pool boiling heat transfer, Appl. Phys. Lett. 100 (24) (2012), 241603.
[6] F.J. Lesage, J.S. Cotton, A.J. Robinson, Analysis of quasi-static vapour bubble shape during growth and departure, Phys. Fluids 25 (6) (2013), 067103.
[7] G. Son, V.K. Dhir, N. Ramanujapu, Dynamics and heat transfer associated with a single bubble during nucleate boiling on a horizontal surface, J. Heat Transf. 121 (3) (1999) 623–631.
[8] A. Mukherjee, S.G. Kandlikar, Numerical study of single bubbles with dynamic contact angle during nucleate pool boiling, Int. J. Heat Mass Transf. 50 (1–2) (2007) 127–138.
[9] Z. Zhou, J. Shi, H.-H. Chen, S.R. Schafer, C.-L. Chen, Two-phase flow over flooded micro-pillar structures with engineered wettability pattern, Int. J. Heat Mass Transf. 71 (2014) 593–605.
[10] Z. Zhao, J. Zhang, D. Jia, K. Zhao, X. Zhang, P. Jiang, Thermal performance analysis of pool boiling on an enhanced surface modified by the combination of microstructures and wetting properties, Appl. Therm. Eng. 117 (2017) 417–426.
[11] Y.-T. Mu, L. Chen, Y.-L. He, Q.-J. Kang, W.-Q. Tao, Nucleate boiling performance evaluation of cavities at mesoscale level, Int. J. Heat Mass Transf. 106 (2017) 708–719.
[12] A. Xu, W. Shyy, T. Zhao, Lattice boltzmann modeling of transport phenomena in fuel cells and flow batteries, Acta Mech. Sinica 33 (3) (2017) 555–574.
[13] H. Huang, M. Sukop, X.-Y. Lu, Multiphase Lattice Boltzmann Methods: Theory and Application, John Wiley & Sons, 2015.
[14] X. Shan, H. Chen, Lattice boltzmann model for simulating flows with multiple phases and components, Phys. Rev. E 47 (3) (1993) 1815.
[15] A. Scagliarini, L. Biferale, M. Sbragaglia, K. Sugiyama, F. Toschi, Lattice boltzmann methods for thermal flows: Continuum limit and applications to compressible rayleigh–taylor systems, Phys. Fluids 22 (5) (2010), 055101.
[16] A. Márkus, G. Házi, Simulation of evaporation by an extension of the pseudopotential lattice boltzmann method: A quantitative analysis, Phys. Rev. E 83 (4) (2011), 046705.
[17] L. Biferale, P. Perlekar, M. Sbragaglia, F. Toschi, Convection in multiphase fluid flows using lattice boltzmann methods, Phys. Rev. Lett. 108 (10) (2012), 104502.
[18] S. Gong, P. Cheng, A lattice boltzmann method for simulation of liquid–vapor phase-change heat transfer, Int. J. Heat Mass Transf. 55 (17) (2012) 4923–4927.
[19] Q. Li, Q.-J. Kang, M.M. Francois, Y.-L. He, K.-H. Luo, Lattice boltzmann modeling of boiling heat transfer: The boiling curve and the effects of wettability, Int. J. Heat Mass Transf. 85 (2015) 787–796.
[20] W.-Z. Fang, L. Chen, Q.-J. Kang, W.-Q. Tao, Lattice boltzmann modeling of pool boiling with large liquid-gas density ratio, Int. J. Therm. Sci. 114 (2017) 172–183.
[21] X. Chang, H. Huang, X.-Y. Lu, Thermal lattice boltzmann study of three-dimensional bubble growth in quiescent liquid, Comput. Fluids 159 (2017) 232–242.
[22] S. Gong, P. Cheng, Direct numerical simulations of pool boiling curves including heater's thermal responses and the effect of vapor phase's thermal conductivity, Int. Commun. Heat Mass Transf. 87 (2017) 61–71.
[23] L. Dong, S. Gong, P. Cheng, Direct numerical simulations of film boiling heat transfer by a phase-change lattice boltzmann method, Int. Commun. Heat Mass Transf. 91 (2018) 109–116.
[24] A. Márkus, G. Házi, On pool boiling at microscale level: the effect of a cavity and heat conduction in the heated wall, Nucl. Eng. Des. 248 (2012) 238–247.
[25] S. Gong, P. Cheng, Two-dimensional mesoscale simulations of saturated pool boiling from rough surfaces. part ii: Bubble interactions above multi-cavities, Int. J. Heat Mass Transf. 100 (2016) 938–948.
[26] Q. Li, Y. Yu, P. Zhou, H. Yan, Enhancement of boiling heat transfer using hydrophilic-hydrophobic mixed surfaces: a lattice boltzmann study, Appl. Therm. Eng. 132 (2018) 490–499.
[27] V.K. Dhir, Mechanistic prediction of nucleate boiling heat transfer–achievable or a hopeless task?, J Heat Transf. 128 (1) (2006) 1–12.
[28] A. Márkus, G. Házi, Numerical simulation of the detachment of bubbles from a rough surface at microscale level, Nucl. Eng. Des. 248 (2012) 263–269.
[29] X. Shan, G. Doolen, Multicomponent lattice-boltzmann model with interparticle interaction, J. Stat. Phys. 81 (1–2) (1995) 379–393.
[30] E. Ezzatneshan, Study of surface wettability effect on cavitation inception by implementation of the lattice boltzmann method, Phys. Fluids 29 (11) (2017), 113304.
[31] A.L. Kupershtokh, D.A. Medvedev, Lattice boltzmann equation method in electrohydrodynamic problems, J. Electrostat. 64 (7–9) (2006) 581–585.
[32] P. Yuan, L. Schaefer, Equations of state in a lattice boltzmann model, Phys. Fluids 18 (4) (2006), 042101.
[33] A.J. Wagner, C.M. Pooley, Interface width and bulk stability: requirements for the simulation of deeply quenched liquid-gas systems, Phys. Rev. E 76 (4) (2007), 045702.
[34] B. Bunner, G. Tryggvason, Dynamics of homogeneous bubbly flows part 1. Rise velocity and microstructure of the bubbles, J. Fluid Mech. 466 (2002) 17–52.
[35] N.S. Martys, H. Chen, Simulation of multicomponent fluids in complex three-dimensional geometries by the lattice boltzmann method, Phys. Rev. E 53 (1) (1996) 743.
[36] D.M. Anderson, G.B. McFadden, A.A. Wheeler, Diffuse-interface methods in fluid mechanics, Annu. Rev. Fluid Mech. 30 (1) (1998) 139–165.
[37] L. Li, C. Chen, R. Mei, J.F. Klausner, Conjugate heat and mass transfer in the lattice boltzmann equation method, Phys. Rev. E 89 (4) (2014), 043308.
[38] G. Pareschi, N. Frapolli, S.S. Chikatamarla, I.V. Karlin, Conjugate heat transfer with the entropic lattice boltzmann method, Phys. Rev. E 94 (1) (2016), 013305.
[39] Q. Zou, X. He, On pressure and velocity boundary conditions for the lattice boltzmann bgk model, Phys. Fluids 9 (6) (1997) 1591–1598.
[40] S. Gong, P. Cheng, Lattice boltzmann simulation of periodic bubble nucleation, growth and departure from a heated surface in pool boiling, Int. J. Heat Mass Transf. 64 (2013) 122–132.
[41] P. Griffith, J.D. Wallis, The role of surface conditions in nucleate boiling, Chem. Eng. Prog. Symp. Ser. 56 (1960) 49–63.
[42] Y.Y. Hsu, On the size range of active nucleation cavities on a heating surface, J. Heat Transf. 84 (3) (1962) 207–213.